Na^+/H^+ antiporter activity by respiratory complex I controls mitochondrial Δψ and is impaired in LHON disease

Pablo Hernansanz-Agustín[1,2]*, Yolanda Martí-Mateos[1], Enrique Calvo[1,3], Jesús Vázquez[1,3], José Antonio Enríquez[1,2]*.

[1]Centro Nacional de Investigaciones Cardiovasculares Carlos III (CNIC); Madrid, E-28029 Spain.

[2]Centro de Investigación Biomédica en Red de Fragilidad y Envejecimiento Saludable.

3Centro de Investigación Biomédica en Red de Enfermedades Cardiovasculares (CIBER-CV). Madrid, Spain

*Corresponding authors. Email: phernansanz@cnic.es and jaenriquez@cnic.es

The mitochondrial electron transport chain (mETC) converts the energy of substrate oxidation into a H^+ electrochemical gradient (Δp), which is composed by an inner mitochondrial membrane (IMM) potential (ΔΨmt) and a pH gradient (ΔpH). So far, ΔΨmt has been assumed to be composed exclusively by H^+. Mitochondrial Ca^{2+} and Na^+ homeostasis, which are essential for cellular function, are controlled by exchangers and antiporters in the inner mitochondrial membrane (IMM). In the last few years, some of them have been identified, except for the mitochondrial Na^+/H^+ exchanger (mNHE). Here, using a rainbow of mitochondrial and nuclear genetic models, we have identified it as, specifically, the P-module of complex I (CI). In turn, its activity creates a Na^+ gradient across the IMM, parallel to ΔpH, which accounts for half of the ΔΨmt in coupled respiring mitochondria. We have also found that a deregulation of this mNHE function in CI, without affecting its enzymatic activity, occurs in Leber hereditary optic neuropathy (LHON), which has profound consequences in ΔΨmt and mitochondrial Ca^{2+} homeostasis and explains the previously unknown molecular pathogenesis of this neurodegenerative disease.

All living organisms rely on the formation of transmembrane potentials to support energy balance, and the maintenance and regulation of these transmembrane potentials are crucial determinants of cell outcomes and homeostasis. Eukaryotes rely on a plasma membrane potential and a mitochondrial inner membrane potential (ΔΨmt), the latter being particularly important for energy production and cell fate determination. The mETC is composed of several complexes and supercomplexes[1]. Mitochondrial complexes I (CI) and II (CII) respectively oxidize NADH and succinate to reduce ubiquinone (CoQ) to ubiquinol. Complex III (CIII) uses ubiquinol to reduce cytochrome c (cyt c), and complex IV (CIV) oxidizes cyt c to reduce O_2 to H_2O. This series of reactions is coupled to the translocation of H^+ by CI, CIII, and CIV across the inner mitochondrial membrane (IMM) to form a H^+-motive force (Δp). Δp, in turn, activates the phosphorylation of ADP to ATP, which is coupled to the electrophoretic entry of H^+ through a fifth complex (CV). Δp is composed of an electrical component (ΔΨmt) and a chemical component (ΔpH)[2], with ΔΨmt accounting for approximately 80% of the total Δp[3].

Mitochondria also contain a panoply of exchangers and antiporters that allow them to maintain respiration, osmolarity, and volume and permit the entry and extrusion of substrates and metabolites[4]. For instance, the mitochondrial Ca^{2+} uniporter (MCU) introduces Ca^{2+} into the mitochondrial matrix and Ca^{2+} is, in turn, extruded by the mitochondrial Na^+/Ca^{2+} exchanger (NCLX) in an electrogenic exchange for 3 Na^+ ions[5]. Mitochondrial Na^+ exit is mediated by a highly active, electroneutral Na^+/H^+ exchanger (NHE) of unknown molecular identity[6].

In the last few years, the relationship between mitochondrial Ca^{2+} imbalance and neurological diseases is becoming clearer[7-9]. LHON is a mitochondrial disorder causing central vision loss at early age by degeneration of the optic nerve and it is produced by mutations in mitochondrial DNA (mtDNA)-encoded CI subunits. Particularly, G11778A, the most common mutation producing LHON, do not show a detectable decrease in CI activity (Figure 1a)[10,11]. Thus, we wondered whether, instead, the molecular pathogenesis could be related to an affectation in mitochondrial Ca^{2+}. We observed that basal mitochondrial Ca^{2+} levels were increased and mitochondrial Ca^{2+} exit rate was lowered altered in LHON cybrids, and that this was not due to lower levels in NCLX amount (Figure 1b-e). Thus, as NCLX activity is coupled to NHE function, we tested whether these defects may be due alterations in the latter. Indeed, we observed that NHE activity in LHON cybrids was abnormally low (Figure 1f). This prompted to question whether other mtDNA mutations or the presence/absence of OXPHOS complexes may also cause a decrease in NHE activity. To note, as decreases in CIII or CIV amounts produce defects in CI assembly[12,13], we tested this in cells expressing *Emericella nidulans* alternative oxidase (AOX) to maintain CI assembly despite the lack of CIII or CIV. We found that only the mutations in CI subunits promoted a decrease in NHE activity, proportionally to the level of mutated DNA (mutation in ND6 is in a 50% heteroplasmy with $mtDNA^{WT}$; Figure 1g).

CI is composed of three structural modules[14-16]. The N-module mediates NADH oxidation and transfers the electrons to the Q-module, also called the CoQ-reducing module. The energy released by the NADH-CoQ oxidoreduction is transferred to the subunits in the H^+ pumping module, or P-module, which is evolutionarily related to the Na^+/H^+ antiporters of alkaliphilic and halophilic bacteria[17], and it is composed by the mtDNA-encoded subunits. Knockout models of different CI subunits produce similar fold decrease in CI activity, regardless of whether they affect the N-module or the P-module (Extended Data Fig. 1a). In contrast, in the literature contradictory findings can be found regarding their bioenergetic impact[18-21]. We wondered whether quantitative differences in NHE activity could lie behind such contrasting behavior and, surprisingly, we found that the knock-out for the N-module subunit NDUFS4 not only not

showed a decrease as the other CI deficiency models, but an increase in NHE activity (Figure 1h-k).

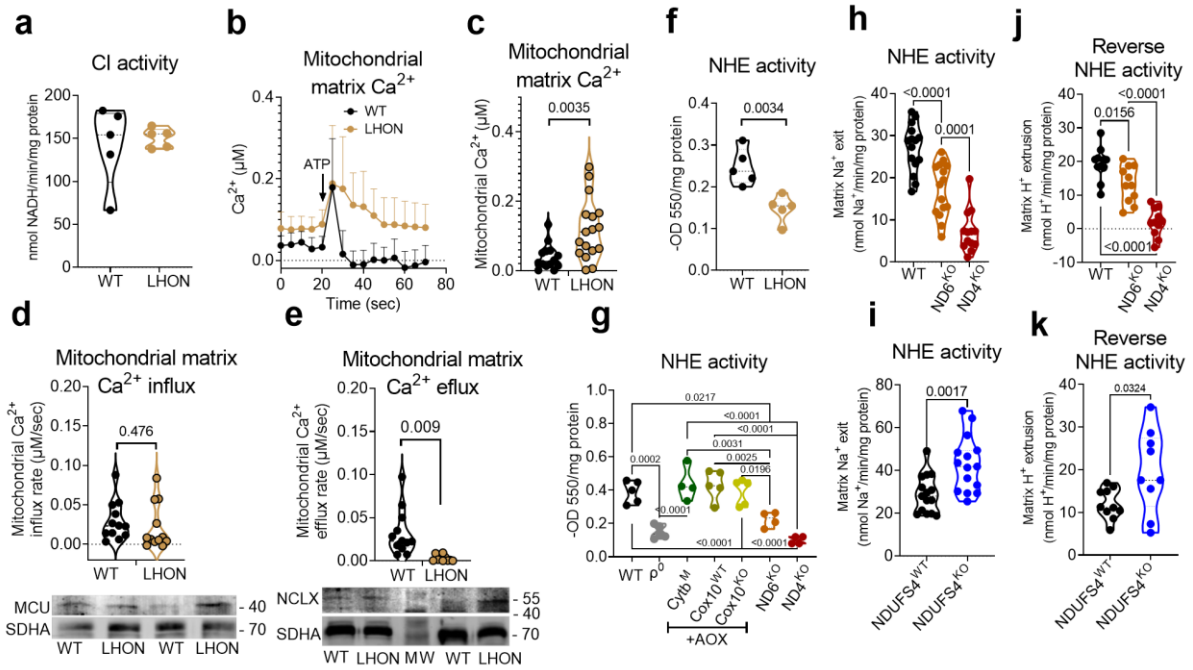

Figure 1. Characterization of CI-dependent NHE activity. (**a**) Rotenone-sensitive NADH-decylubiquinone oxidorectidase activity in LHON vs control mitochondrial membranes. (**b**) Mitochondrial Ca^{2+} levels in LHON vs control cells before and after addition of ATP. (**c**) Mitochondrial Ca^{2+} basal levels in LHON vs control cells. (**d**) Mitochondrial Ca^{2+} influx rate in LHON vs control cells. Inset: western blot of mitochondrial extracts showing the mitochondrial calcium uniporter (MCU) levels and a loading control (SDHA). (**e**) Mitochondrial Ca^{2+} efflux rate in LHON vs control cells. Inset: western blot of mitochondrial extracts showing NCLX levels, a loading control (SDHA) and the ladder. (**f**) Passive NHE activity in LHON vs control mitochondria. (**g**) Passive NHE activity in control, ρ0, $Cytb^{M}$+AOX, $Cox10^{WT}$+AOX, $Cox10^{KO}$+AOX, $ND6^{KO}$ and $ND4^{KO}$ mitochondria. (**h**) Mitochondrial matrix Na^{+} extrusion measured with SBFI-AM in $mtDNA^{WT}$, $ND6^{KO}$ and $ND4^{KO}$ intact mitochondria respiring on succinate. (**i**) Mitochondrial matrix Na^{+} extrusion measured with SBFI-AM in $NDUFS4^{WT}$ and $NDUFS4^{KO}$ intact mitochondria respiring on succinate. (**j**) Mitochondrial matrix H^{+} extrusion measured with BCECF-AM in $mtDNA^{WT}$, $ND6^{KO}$ and $ND4^{KO}$ intact mitochondria respiring on succinate. (**k**) Mitochondrial matrix H^{+} extrusion measured with BCECF-AM in $NDUFS4^{WT}$ and $NDUFS4^{KO}$ intact mitochondria respiring on succinate.

Consistent with ND6 mutant mtDNA being in heteroplasmy[18,20], $ND6^{KO}$ cells showed residual CI assembly with respect to control isogenic cybrid cells (WT), whereas $ND4^{KO}$ cells contained no detectable levels of assembled CI (Figure 2a). The remaining mitochondrial complexes showed a redistributed pattern on blue-native gel electrophoresis (BNGE) consistent with reduced levels of CI-containing supercomplexes (Figure 2a). In contrast, $NDUFS4^{KO}$ MAFs showed slightly faster migration of CI-containing supercomplexes than $NDUFS4^{WT}$ MAFs, reflecting the assembly of CI with only the Q- and P-modules (Figure 2b). Thus, $NDUFS4^{KO}$ has a higher NHE activity with its CI P-module conserved. In contrast to other CI defects in the P-module ($ND4^{KO}$ and $ND6^{KO}$ models) and the LHON causing point mutation in the mtDNA encoded ND4 protein, produces a specific decrease in NHE activity. This, together with the fact that the mtDNA-encoded CI subunits are related to bacterial NHE and that the *E.coli* CI may act as a NHE[22-24], strongly support that CI P-module is a bona-fide NHE in mitochondria. Indeed, this is supported by *in vitro* data using isolated bovine CI reconstituted in liposomes[25].

As we now had a loss- and gain-in-function models of NHE, we wondered what the bioenergetic consequences would be, if any, in these cell models (ND4^{KO}, ND6^{KO} vs NDUFS4^{KO}). In line with a loss of CI activity, all cell models, including wild type cells chronically exposed to low-dose of the Q-module-binding inhibitor rotenone (Chronic Rot), showed an increase in combined CII+III activity compared with untreated or vehicle-treated mtDNA^{WT} cells (Figure 2c-f and Extended Data Figure 1b, summarized in Table S1). Increased CII+III activity is a well-known consequence of Fgr kinase activity in these models[18]. In contrast, isolated CIV activity was elevated only in ND4^{KO} and NDUFS4^{KO} cells (Figure 2g-j and Extended Data Figure 1c), while CV activity, in forward or reverse mode, was higher only in NDUFS4^{KO} cells (Extended Data Figure 1d-e, summarized in Table S1). Analysis of oxygen consumption by permeabilized cells respiring on CI, CII, or CIV substrates revealed that CI-dependent respiration was much lower in ND4^{KO}, ND6^{KO}, and Chronic Rot cells with respect to their wild type or vehicle-treated counterparts but was surprisingly unaltered in NDUFS4^{KO} cells (CI in Figure 3a-c and Extended Data Figure 2a). In the presence of CII substrates, independently of the presence of ADP, respiration rates were higher in all cell models except for ND6^{KO} (CII and CII+ADP in Figure 3a-c and Extended Data Figure 2a). CIV-dependent

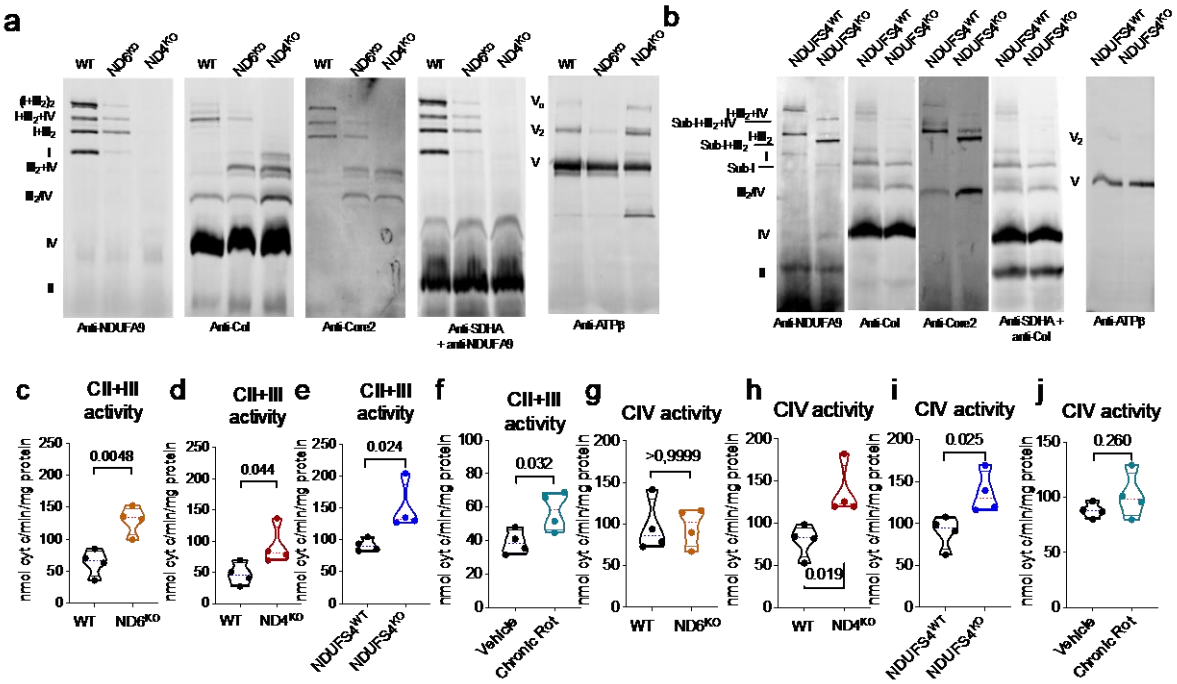

Figure 2. Characterization of CI-deficiency models. (**A**) Blue-native electrophoresis (BN-PAGE) of mitochondria from mtDNA^{WT}, ND6^{KO}, and ND4^{KO} cybrid cell lines (n=3 per genotype) immunoblotted to detect subunits of CI (Anti-NDUFA9), CIV (Anti-CoI), CIII (Anti-Core2), CII (Anti-SDHA), and CV (Anti-ATPβ). (**B**) BN-PAGE of mitochondria from NDUFS4^{WT} and NDUFS4^{KO} MAFs (n=2) blotted against the same epitopes as in (**A**). The lateral labels in (**A**) and (**B**) indicate the migrated positions of all detected complexes and supercomplexes. (**C**) Antimycin A (AA)-sensitive succinate-cyt c oxidoreductase activity in mtDNA^{WT} and ND6^{KO} mitochondrial membranes. (**D**) AA-sensitive succinate-cyt c oxidoreductase activity in mtDNA^{WT} and ND4^{KO} mitochondrial membranes. (**E**) AA-sensitive succinate-cyt c oxidoreductase activity in NDUFS4^{WT} and NDUFS4^{KO} mitochondrial membranes. (**F**) AA-sensitive succinate-cyt c oxidoreductase activity in mtDNA^{WT} mitochondrial membranes from cells treated for 6 h with either vehicle or 250 nM rotenone (Chronic Rot). (**G**) Potassium cyanide (KCN)-sensitive cyt c oxidase activity in mtDNA^{WT} and ND6^{KO} mitochondrial membranes. (**H**) KCN-sensitive cyt c oxidase activity in mtDNA^{WT} and ND4^{KO} mitochondrial membranes. (**I**) KCN-sensitive cyt c oxidase activity in NDUFS4^{WT} and NDUFS4^{KO} mitochondrial membranes. (**J**) KCN-sensitive cyt c oxidase activity in mtDNA^{WT} mitochondrial membranes from cells treated for 6 h with either vehicle or 250 nM rotenone (Chronic Rot).

respiration was similar in mtDNA^{WT} and ND6^{KO} cells and elevated in ND4^{KO} and NDUFS4^{KO} cells (CIV in Figure 3a-c), resembling isolated CIV activity (Figure 2g-j and Extended Data Figure 2c).

Analysis of ΔΨmt revealed that ND6^{KO} mitochondria were depolarized relative to isogenic controls respiring on any substrate (Figure 3d). In contrast, ND4^{KO} mitochondria were depolarized only when respiring on CI substrates, showing normal mitochondrial membrane polarization when respiring on CII and CIV substrates (Figure 3e). NDUFS4^{KO} mitochondria were not depolarized by CI substrates and were hyperpolarized by CII and CIV substrates (Figure 3f). The mitochondria of Chronic-Rot–treated cells were depolarized by CI substrates and hyperpolarized by CII substrates (Extended Data Figure 2b-d). The different cell models thus show apparent contradictory behaviors. What most called our attention was the discrepancy between elevated CII+III and CIV activities and weaker or unaffected mitochondrial membrane polarization in ND6^{KO} and ND4^{KO} cells supplied with CII and CIV substrates (Figure 2c, d, g and h, CII and CIV insets in Figure 3d-e). This contrasted with NDUFS4^{KO} and Chronic Rot

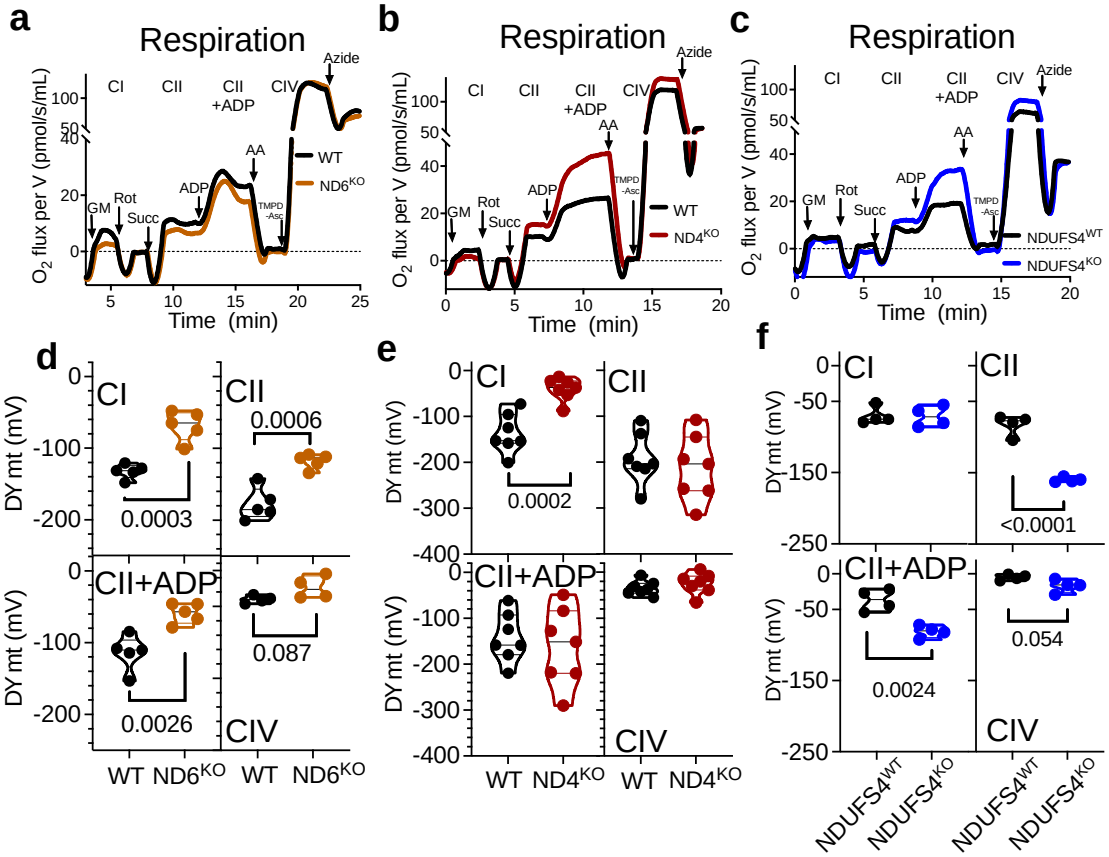

Figure 3. Bioenergetic characterization of the ND6^{KO}, ND4^{KO,} and NDUFS4^{KO} cell lines. (**a**) Oxygen consumption rates in mtDNA^{WT} and ND6^{KO} permeabilized cells (n=5). (**b**) Oxygen consumption rates in mtDNA^{WT} and ND4^{KO} permeabilized cells (n=7). (**c**) Oxygen consumption rates in NDUFS4^{WT} and NDUFS4^{KO} permeabilized cells (n=4). GM, glutamate/malate; Rot, 1 µM rotenone; Succ, succinate; ADP, adenosine di-phosphate; AA, 1 µM antimycin A; TMPD+Asc, N,N,N′,N′-tetramethyl-p-phenylenediamine + ascorbate; Azide, 50 mM, sodium azide. CI denotes CI-dependent respiration, CII denotes CII-dependent respiration, CII+ADP denotes CII+ADP-dependent respiration, and CIV denotes CIV-dependent respiration. (**d-f**) Calibrated TMRM signal in mtDNA^{WT}, ND6^{KO} (**d**), ND4^{KO} (**e**) and NDUFS4^{KO} cells (**f**), providing the CI-dependent ΔΨmt (Panel CI in **d-f**), CII-dependent ΔΨmt (Panel CII in **d-f**), CII+ADP-dependent ΔΨmt (Panel CII+ADP in **d-f**), and CIV-dependent ΔΨmt (Panel CIV in **d-f**).

cells, which also showed elevated CII+III activity (and also elevated CIV activity in the case of NDUFS4^{KO} cells), but in this case accompanied by CII-dependent mitochondrial hyperpolarization (and CIV-dependent hyperpolarization in NDUFS4^{KO} cells; Figure 2e, i and Figure 3f, Figure 2f-j and Extended Data Figure 2b-d), despite an even higher forward CV activity in the case of NDUFS4^{KO} cells (Extended Data Figure 1d). To exclude an effect of artifacts arising from the use of permeabilized cells, we repeated the same experiments with isolated mitochondria. The results were the same in all cases except for ND6^{KO} mitochondria, in which respiration rates and ΔΨmt were like those in mitochondria isolated from isogenic wild type cells (Extended Data Figure 3, summarized in Table S1). These results show that knockout models for different CI subunits have distinct bioenergetic footprints under non-CI substrates.

This variable behavior has several possible explanations. We first pondered the possible involvement of mitochondrial volume, H^+ leak, or mitochondrial transition pore (MTP) opening. However, none of these parameters was changed in ND6^{KO} or ND4^{KO} mitochondria with respect to their isogenic control (Extended Data Figure 4). In line with previous reports[20,26], a proteomics analysis of isolated mitochondria from ND6^{KO}, ND4^{KO}, and NDUFS4^{KO} cells showed a pronounced reduction in most CI subunits in ND4^{KO} and ND6^{KO} cells, contrasting with unaltered levels of P-module subunits in NDUFS4^{KO} cells (Extended Data Figure 5a and e). All the cell models had a similar protein content of other mitochondrial complex subunits (Extended Data Fig 5b-d and Fig. 5f-h). In a false discovery rate analysis, the only difference detected between NDUFS4^{KO} MAFs and the ND6^{KO} and ND4^{KO} lines was the presence in the cybrid lines of mitochondrial medium-chain specific acyl-CoA dehydrogenase (ACADM) (Extended Data Figure 5i-k). However, this fatty acid oxidation enzyme locates in the mitochondrial matrix, whereas the discrepancies we observed are related to the IMM ΔΨmt provoked by CII and CIV substrates. We therefore discarded an involvement of ACADM in the generation and maintenance of ΔΨmt.

Strikingly, frozen-thawed-permeabilized ND6^{KO} and ND4^{KO} mitochondria supplied with CII and CIV substrates had markedly higher oxygen consumption rates relative to isogenic controls than observed with intact ND6^{KO} and ND4^{KO} mitochondria (compare Fig. 4a and b with Extended Data Figure 3a and b). This finding suggested that the distinct bioenergetic footprints of the different CI subunit knockout models might be determined by IMM integrity. We first tested whether the same sample treated with different CI inhibitors may affect equally NHE activity. Only high doses of rotenone were able to decrease NHE activity, in contrast to the N-module inhibitor DPI (Extended Data Figure 6 a-b), which is compatible with the fact that rotenone is also able to bind ND4 at high doses, potentially inhibiting CI NHE[27]. Accordingly, CI activation state only increased NHE function, as occurred with NDUFS4^{KO}, and in contrast to the two other CI deficiency models (Extended Data Figure 6 c-e), which is also in agreement with previous *in vitro* data[25].

As ND6^{KO} and ND4^{KO} did not show the expected hyperpolarization under CII and/or CIV substrates, we decided to measure H^+ pumping in the same conditions, in all CI deficiency models, as it could be a result of lower H^+ ejected by CIII and/or CIV. As expected, H^+ pumping was lower in all three of the knockout lines when they were reliant on CI substrates (Extended Data Figure 6f, g, i and j). However, with CII substrates, ND6^{KO} and ND4^{KO} mitochondria showed higher H^+ pumping than isogenic controls, resembling NDUFS4^{KO} mitochondria (Extended Data Figure 6f, h, i and k). This finding fits well with our data showing higher CII+III activity in all CI-deficiency models (compare Extended Data Figure 6h and k with Fig. 2c-f). However, the absence of hyperpolarization in ND6^{KO} and ND4^{KO} mitochondria occurred despite

their showing higher H^+ pumping. This intriguing contradiction opens the possibility that CI P-module-dependent NHE activity influences ΔΨmt, so that it is governed not only by a H^+ gradient, but also by a Na^+ gradient.

To evaluate this hypothesis, we tackled this by three different approaches. First, we recorded ΔΨmt in wild type and $ND4^{KO}$ mitochondria, supplied with CII substrates and upon the addition of the chemical Na^+/H^+ exchanger monensin to chemically restore the NHE function in isolated mitochondria. Whereas nigericin, a chemical K^+/H^+ exchanger, promoted hyperpolarization in isolated wild type mitochondria (Extended Data Figure 6l), monensin did not (Extended Data Figure 6m and n). In contrast, both drugs supported hyperpolarization of $ND4^{KO}$ mitochondria (Extended Data Figure 6l and m), indicating that the restoration of a Na^+ gradient by monensin addition contributed to the establishment of ΔΨmt in $ND4^{KO}$ mitochondria. No similar phenomenon was observed with $NDUFS4^{KO}$ mitochondria (Extended Data Figure 6n).

Second, we measured respiration rates and ΔΨmt in intact wild type mitochondria maintained in an osmotically compensated, Na^+-free buffer. The absence of Na^+ slightly decreased the respiration rate and promoted mitochondrial depolarization by a third or a half, depending on the substrate conditions (Figure 4c and Extended Data Figure 6o). Mouse heart mitochondria behaved similarly (Extended Data Figure 6q-r). In parallel, the absence of Na^+ promoted apparently higher CI- and CII-dependent H^+ pumping, which we interpreted as the consequence of an inoperative NHE, unable to dissipate ΔpH (Figure 4d and e). None of these phenomena was observed in $ND4^{KO}$ mitochondria (Figure 4f-h and Extended Data Figure 6p), pointing to a role of the CI NHE-dependent formation of ΔΨmt, possibly reliant on a Na^+ gradient. Within this approach we also compared respiration rates and ΔΨmt between wild type and $ND4^{KO}$ mitochondria in the absence of Na^+. Under these conditions, $ND4^{KO}$ mitochondria showed even higher respiration (compare Extended Data Figure 6s and Extended Data Figure 3b) and, more importantly, hyperpolarization with respect to $mtDNA^{WT}$ under CII and CIV substrates (Figure 4t-w). This outcome resembled the bioenergetic footprint of $NDUFS4^{KO}$ and Chronic Rot mitochondria maintained in Na^+-containing buffer (Table S1), indicating that the build-up of a Na^+ gradient-dependent ΔΨmt specifically in wild type mitochondria was masking the effect of higher CII+CIII activity and H^+ pumping on respiration and ΔΨmt in the $ND6^{KO}$ and $ND4^{KO}$ cell models, which may be unable to form a Na^+ gradient-dependent ΔΨmt.

In a third approach, we directly measured the mitochondrial Na^+ gradient in isolated mitochondria. For respiration driven by CI or CII substrates, the Na^+ gradient in $ND6^{KO}$ and $ND4^{KO}$ mitochondria was below-control in proportion to the level of assembled CI (Figure 4i and j). In contrast, the Na^+ gradient in $NDUFS4^{KO}$ mitochondria was unaffected (Figure 4k and

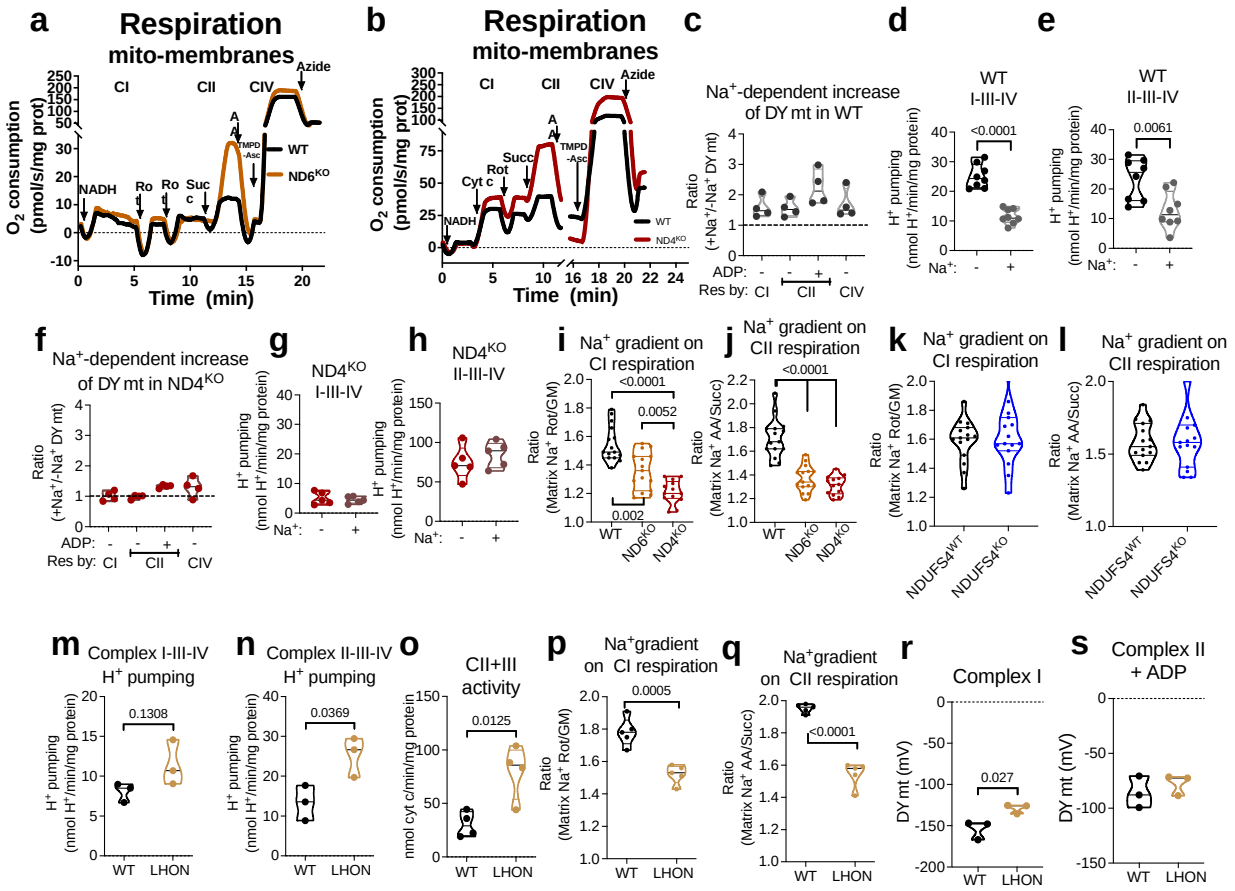

Figure 4. Mitochondrial Na^+ gradient controls ΔΨmt and is lowered in LHON. (**a**) Oxygen consumption rates in $mtDNA^{WT}$ and $ND6^{KO}$ frozen-thawed-permeabilized mitochondria in the presence of cyt c (n=3). (**b**) Oxygen consumption rates in $mtDNA^{WT}$ and $ND4^{KO}$ frozen-thawed-permeabilized mitochondria in the presence of cyt c (n=3). (**c**) Relative contribution of Na^+ to ΔΨmt in $mtDNA^{WT}$ mitochondria respiring on different substrates, calculated as the ratio of the calibrated TMRM signal in Na^+-containing buffer to that in Na^+-free buffer. (**d-e**) Mitochondrial matrix H^+ pumping measured from the BCEFC-AM signal in $mtDNA^{WT}$ isolated mitochondria respiring on CI (**d**) or CII (**e**) substrates in Na^+-containing and Na^+-free buffer. (**f**) Relative contribution of Na^+ to ΔΨmt in $ND4^{KO}$ mitochondria respiring on CI, CII, CII+ADP, or CIV substrates, calculated as the ratio of the calibrated TMRM signal in Na^+-containing to that in Na^+-free buffer. (**g-h**) Mitochondrial matrix H^+ pumping measured from the BCEFC-AM signal in $ND4^{KO}$ isolated mitochondria respiring on CI (**g**) or CII (**h**) substrates in Na^+-containing and Na^+-free buffer. (**i-j**) Na^+ gradient in $mtDNA^{WT}$, $ND6^{KO}$, and $ND4^{KO}$ isolated mitochondria incubated with SBFI-AM and respiring on GM (**i**) or succinate (**j**), calculated as the ratio of the matrix Na^+ concentrations determined after and before the addition of rotenone (**i**) or antimycin A (**j**). (**k-l**) Na^+ gradient in $NDUFS4^{WT}$ and $NDUFS4^{KO}$ isolated mitochondria incubated with SBFI-AM and respiring on GM (**k**) or succinate (**l**), calculated as the ratio of the matrix Na^+ concentrations determined after and before the addition of rotenone (**k**) or antimycin A (**l**). (**m-n**) Mitochondrial matrix H^+ pumping measured from the BCEFC-AM signal in control vs LHON isolated mitochondria respiring on CI (**m**) or CII (**n**) substrates in Na^+-containing buffer. (**o**) Antimycin A-sensitive succinate-cytochrome c oxidoreductase activity in LHON vs control mitochondrial membranes. (**p-q**) Na^+ gradient in control versus LHON isolated mitochondria incubated with SBFI-AM and respiring on GM (**p**) or succinate (**q**), calculated as the ratio of the matrix Na^+ concentrations determined after and before the addition of rotenone (**p**) or antimycin A (**q**). (**r-s**) Calibrated TMRM signal in control versus LHON respiring with CI (**r**) or CII+ADP (**s**) substrates.

l), indicating that formation of the Na^+ gradient requires a fully assembled CI P-module. Measurement of the cytosolic and mitochondrial Na^+ content in intact cells confirmed that (1) there are different concentrations of Na^+ in the cytosol and mitochondria (Extended Data Figure 7a), that (2) total Na^+ content was similar in all the cell models (Extended Data Figure 7b) and (3) that the transmitochondrial Na^+ gradient exists not only in isolated mitochondria, but also in a similar magnitude in intact cells (Extended Data Figure 7b).

From the measurements taken throughout this study, we calculate that for respiration driven by CI or CII substrates the Na^+ gradient contributes around one third of the total ΔΨmt (Table S2)). However, when CV is activated by the presence of ADP (state 3) and partially dissipates ΔpH, the electrical contribution of the Na^+ gradient reaches approximately half of the ΔΨmt (Table S2). The mitochondrial Na^+ gradient thus either parallels the mitochondrial H^+ gradient (compare $mtDNA^{WT}$ in Extended Data Figure 7d and e with $mtDNA^{WT}$ in Figure 4i and j) or even surpasses it (compare $NDUFS4^{WT}$ in Extended Data Figure 7f and g with $NDUFS4^{WT}$ in Figure 4k and l). This near-equal contribution of the Na^+ gradient and the H^+ gradient to ΔΨmt in coupled-respiring mitochondria predicts that mutations of key CI P-module residues, altering CI NHE activity may alter ΔΨmt, independently of their CI NADH-CoQ oxidoreductase activity and H^+ pumping capacity. Indeed, LHON mitochondria showed no differences in H^+ pumping capacity under CI substrates and higher values for CII-dependent respiration (Figure 4m and n), which fits well with CI (Figure 1a) and CII+III activities (Figure 4o). In accordance with a lesser NHE activity and its contribution to the build-up of ΔΨmt, LHON mitochondria showed lower Na^+ gradient under CI and CII substrates (Figure 4o and p), depolarized mitochondria under CI substrates and absence of hyperpolarization with CII substrates (Figure 4q and r). This was confirmed by measuring ΔΨmt in LHON intact cybrids (Extended Data Figure 7h).

The results reported here demonstrate that CI operates as an NHE in isolated mitochondria and intact cells, regardless if CI is in its active conformation, and that doing that, CI builds up a Na^+ gradient across the IMM that significantly contributes to the ΔΨmt. CI-NHE activity has a H^+-dissipating effect (ΔpH becomes partially substituted by a Na^+ gradient), and this effect allows higher respiration rates at lower levels of CI NADH-CoQ oxidoreductase activity. Indeed, $NDUFS4^{KO}$ mitochondria supplied with CI substrates were able to respire and build up ΔΨmt to a similar extent as their wild type counterparts (CI panel in Figure 3f and l and Extended Data Figure 3f) despite their lower CI activity (Extended Data Figure 1a), highlighting that higher CI-NHE activity (Figure 1i and k, and Extended Data Figure 6e) allows the formation of a mitochondrial Na^+ gradient (Figure 4k) at a lower available H^+ gradient (Extended Data Figure 7f). In parallel, because $ND6^{KO}$ and $ND4^{KO}$ cells were incapable of forming a mitochondrial Na^+ gradient (Figure 4i-j), they were unable to increase mitochondrial respiration or hyperpolarize (Figure 3a-e and Extended Data Figure 3a-e) despite having higher CII+III activity (Figure 2c-d). In other words, the presence of CI-NHE activity and the concomitant formation of a mitochondrial Na^+ gradient enables the control of ΔΨmt, in addition to ΔpH, and a more efficient use of substrates in terms of oxygen consumption. Indeed, a specific deficiency in the CI-NHE function, independently of CI NADH-CoQ oxidoreductase activity, contributes to the molecular mechanism of the m.11778G>A mutation at ND4, responsible for the mtDNA-linked Leber hereditary optic neuropathy, through deregulation of mitochondrial Ca^{2+} homeostasis. The discovery that the Na^+ gradient controls ΔΨmt, together with its tight regulation by a non-canonical NHE function of CI, introduces a new and unexpected layer of regulation to mitochondrial bioenergetics, with extensive implications for neurological physiology and disease.

Main references

1 Hernansanz-Agustin, P. & Enriquez, J. A. Functional segmentation of CoQ and cyt c pools by respiratory complex superassembly. *Free Radic Biol Med* **167**, 232-242 (2021). https://doi.org:10.1016/j.freeradbiomed.2021.03.010

2 Mitchell, P. Coupling of phosphorylation to electron and hydrogen transfer by a chemi-osmotic type of mechanism. *Nature* **191**, 144-148 (1961). https://doi.org:10.1038/191144a0

3 Nicholls, D. G. The influence of respiration and ATP hydrolysis on the proton-electrochemical gradient across the inner membrane of rat-liver mitochondria as determined by ion distribution. *Eur J Biochem* **50**, 305-315 (1974). https://doi.org:10.1111/j.1432-1033.1974.tb03899.x

4 Poburko, D. & Demaurex, N. Regulation of the mitochondrial proton gradient by cytosolic Ca(2)(+) signals. *Pflugers Arch* **464**, 19-26 (2012). https://doi.org:10.1007/s00424-012-1106-y

5 Palty, R. *et al.* NCLX is an essential component of mitochondrial Na+/Ca2+ exchange. *Proc Natl Acad Sci U S A* **107**, 436-441 (2010). https://doi.org:10.1073/pnas.0908099107

6 Hernansanz-Agustin, P. & Enriquez, J. A. Sodium in Mitochondrial Redox Signaling. *Antioxid Redox Signal* (2022). https://doi.org:10.1089/ars.2021.0262

7 Gandhi, S. *et al.* PINK1-associated Parkinson's disease is caused by neuronal vulnerability to calcium-induced cell death. *Mol Cell* **33**, 627-638 (2009). https://doi.org:10.1016/j.molcel.2009.02.013

8 Jadiya, P. *et al.* Impaired mitochondrial calcium efflux contributes to disease progression in models of Alzheimer's disease. *Nat Commun* **10**, 3885 (2019). https://doi.org:10.1038/s41467-019-11813-6

9 Kostic, M. *et al.* PKA Phosphorylation of NCLX Reverses Mitochondrial Calcium Overload and Depolarization, Promoting Survival of PINK1-Deficient Dopaminergic Neurons. *Cell Rep* **13**, 376-386 (2015). https://doi.org:10.1016/j.celrep.2015.08.079

10 Hofhaus, G., Johns, D. R., Hurko, O., Attardi, G. & Chomyn, A. Respiration and growth defects in transmitochondrial cell lines carrying the 11778 mutation associated with Leber's hereditary optic neuropathy. *J Biol Chem* **271**, 13155-13161 (1996). https://doi.org:10.1074/jbc.271.22.13155

11 Larsson, N. G., Andersen, O., Holme, E., Oldfors, A. & Wahlstrom, J. Leber's hereditary optic neuropathy and complex I deficiency in muscle. *Ann Neurol* **30**, 701-708 (1991). https://doi.org:10.1002/ana.410300511

12 Acin-Perez, R. *et al.* Respiratory complex III is required to maintain complex I in mammalian mitochondria. *Mol Cell* **13**, 805-815 (2004). https://doi.org:10.1016/s1097-2765(04)00124-8

13 Guaras, A. *et al.* The CoQH2/CoQ Ratio Serves as a Sensor of Respiratory Chain Efficiency. *Cell Rep* **15**, 197-209 (2016). https://doi.org:10.1016/j.celrep.2016.03.009
14 Agip, A. A., Blaza, J. N., Fedor, J. G. & Hirst, J. Mammalian Respiratory Complex I Through the Lens of Cryo-EM. *Annu Rev Biophys* **48**, 165-184 (2019). https://doi.org:10.1146/annurev-biophys-052118-115704
15 Kampjut, D. & Sazanov, L. A. Structure of respiratory complex I - An emerging blueprint for the mechanism. *Curr Opin Struct Biol* **74**, 102350 (2022). https://doi.org:10.1016/j.sbi.2022.102350
16 Parey, K. *et al.* Cryo-EM structure of respiratory complex I at work. *Elife* **7** (2018). https://doi.org:10.7554/eLife.39213
17 Hamamoto, T. *et al.* Characterization of a gene responsible for the Na+/H+ antiporter system of alkalophilic Bacillus species strain C-125. *Mol Microbiol* **14**, 939-946 (1994). https://doi.org:10.1111/j.1365-2958.1994.tb01329.x
18 Acin-Perez, R. *et al.* ROS-triggered phosphorylation of complex II by Fgr kinase regulates cellular adaptation to fuel use. *Cell Metab* **19**, 1020-1033 (2014). https://doi.org:10.1016/j.cmet.2014.04.015
19 McManus, M. J. *et al.* Mitochondrial DNA Variation Dictates Expressivity and Progression of Nuclear DNA Mutations Causing Cardiomyopathy. *Cell Metab* **29**, 78-90 e75 (2019). https://doi.org:10.1016/j.cmet.2018.08.002
20 Perales-Clemente, E. *et al.* Five entry points of the mitochondrially encoded subunits in mammalian complex I assembly. *Mol Cell Biol* **30**, 3038-3047 (2010). https://doi.org:10.1128/MCB.00025-10
21 Valsecchi, F. *et al.* Metabolic consequences of NDUFS4 gene deletion in immortalized mouse embryonic fibroblasts. *Biochim Biophys Acta* **1817**, 1925-1936 (2012). https://doi.org:10.1016/j.bbabio.2012.03.006
22 Batista, A. P., Marreiros, B. C. & Pereira, M. M. Decoupling of the catalytic and transport activities of complex I from Rhodothermus marinus by sodium/proton antiporter inhibitor. *ACS Chem Biol* **6**, 477-483 (2011). https://doi.org:10.1021/cb100380y
23 Castro, P. J., Silva, A. F., Marreiros, B. C., Batista, A. P. & Pereira, M. M. Respiratory complex I: A dual relation with H(+) and Na(+)? *Biochim Biophys Acta* **1857**, 928-937 (2016). https://doi.org:10.1016/j.bbabio.2015.12.008
24 Stolpe, S. & Friedrich, T. The Escherichia coli NADH:ubiquinone oxidoreductase (complex I) is a primary proton pump but may be capable of secondary sodium antiport. *J Biol Chem* **279**, 18377-18383 (2004). https://doi.org:10.1074/jbc.M311242200
25 Roberts, P. G. & Hirst, J. The deactive form of respiratory complex I from mammalian mitochondria is a Na+/H+ antiporter. *J Biol Chem* **287**, 34743-34751 (2012). https://doi.org:10.1074/jbc.M112.384560
26 Sterky, F. H. *et al.* Altered dopamine metabolism and increased vulnerability to MPTP in mice with partial deficiency of mitochondrial complex I in dopamine neurons. *Hum Mol Genet* **21**, 1078-1089 (2012). https://doi.org:10.1093/hmg/ddr537
27 Kampjut, D. & Sazanov, L. A. The coupling mechanism of mammalian respiratory complex I. *Science* **370** (2020). https://doi.org:10.1126/science.abc4209
28 Fernandez-Vizarra, E. *et al.* Isolation of mitochondria for biogenetical studies: An update. *Mitochondrion* **10**, 253-262 (2010). https://doi.org:10.1016/j.mito.2009.12.148
29 Hernansanz-Agustin, P. *et al.* Na(+) controls hypoxic signalling by the mitochondrial respiratory chain. *Nature* **586**, 287-291 (2020). https://doi.org:10.1038/s41586-020-2551-y

30 Morava, E. *et al.* Clinical and biochemical characteristics in patients with a high mutant load of the mitochondrial T8993G/C mutations. *Am J Med Genet A* **140**, 863-868 (2006). https://doi.org:10.1002/ajmg.a.31194

31 Wittig, I., Braun, H. P. & Schagger, H. Blue native PAGE. *Nat Protoc* **1**, 418-428 (2006). https://doi.org:10.1038/nprot.2006.62

32 Vives-Bauza, C., Yang, L. & Manfredi, G. Assay of mitochondrial ATP synthesis in animal cells and tissues. *Methods Cell Biol* **80**, 155-171 (2007). https://doi.org:10.1016/S0091-679X(06)80007-5

33 Dlaskova, A., Hlavata, L., Jezek, J. & Jezek, P. Mitochondrial Complex I superoxide production is attenuated by uncoupling. *Int J Biochem Cell Biol* **40**, 2098-2109 (2008). https://doi.org:10.1016/j.biocel.2008.02.007

34 Douglas, M. G. & Cockrell, R. S. Mitochondrial cation-hydrogen ion exchange. Sodium selective transport by mitochondria and submitochondrial particles. *J Biol Chem* **249**, 5464-5471 (1974).

35 Navarro, P. & Vazquez, J. A refined method to calculate false discovery rates for peptide identification using decoy databases. *J Proteome Res* **8**, 1792-1796 (2009). https://doi.org:10.1021/pr800362h

36 Bonzon-Kulichenko, E., Garcia-Marques, F., Trevisan-Herraz, M. & Vazquez, J. Revisiting peptide identification by high-accuracy mass spectrometry: problems associated with the use of narrow mass precursor windows. *J Proteome Res* **14**, 700-710 (2015). https://doi.org:10.1021/pr5007284

37 Trevisan-Herraz, M. *et al.* SanXoT: a modular and versatile package for the quantitative analysis of high-throughput proteomics experiments. *Bioinformatics* **35**, 1594-1596 (2019). https://doi.org:10.1093/bioinformatics/bty815

38 Garcia-Marques, F. *et al.* A Novel Systems-Biology Algorithm for the Analysis of Coordinated Protein Responses Using Quantitative Proteomics. *Mol Cell Proteomics* **15**, 1740-1760 (2016). https://doi.org:10.1074/mcp.M115.055905

Acknowledgments

We thank Dr. Sara Cogliati (CMBSO, UAM-CSIC) for helping with TEM imaging; Andrea Curtabbi, Carmen Morales Vidal, Dr. Demetrio Julián Santiago Castillo, Dr. Silvia Priori (CNIC), Dr. Eduardo Rial (CIB-CSIC) for fruitful discussion, and M. M. Muñoz-Hernandez, R. Martínez de Mena, E.R. Martínez Jiménez, and C. Jiménez for technical assistance.

Author contributions

Conceptualization: PHA and JAE. Methodology: PHA, YMM (Opa1 western blot) and EC (Proteomics). Investigation: PHA. Funding acquisition: JAE and JV. Project administration: JAE. Writing: PHA and JAE. Writing – review & editing: PHA, YMM, EC, JV and JAE.

Competing interests' declaration

Authors declare that they have no competing interests.

Additional information

Funding: This study was supported by competitive grants from the *Ministerio de Ciencia e Innovación* (MCIN) RTI2018-099357-B-I00, and CIBERFES (CB16/10/00282), Human Frontier Science Program (grant RGP0016/2018), and Leducq Transatlantic Networks (17CVD04) to JAE. PHA is supported by a JdC IJC2020-042679-I, YMM is supported by a FPI-SO fellowship PRE2018-083478. The CNIC is supported by the ISCIII, the MCIN and the Pro CNIC Foundation, and is a Severo Ochoa Center of Excellence

Data and materials availability: All data are available in the main text or the supplementary materials. Cell lines will be available under a materials transfer agreement (MTAs).

Extended Data

Materials and methods

Cell culture and treatment

mtDNA^{WT} cybrids, ND6^{KO} cybrids, ND4^{KO} cybrids, hmtDNAWT cybrids, LHON cybrids, NDUFS4^{WT} mouse adult fibroblasts (MAFs), NDUFS4^{KO} MAFs, and human control and LHON cybrids were cultured in DMEM supplemented with 5% heat-inactivated FBS, 100 U/mL penicillin, and 100 µg/mL streptomycin. All cells were correctly recognized from proteomic analysis, CI assembly assessed by Blue Native polyacrylamide gel electrophoresis (BN-PAGE), and CI spectrophotometric activity.

Chronic rotenone (Chronic Rot) treatment consisted of incubating mtDNA^{WT} cybrids with 250 nM rotenone for 4-6 hours. This rotenone concentration was maintained throughout the detachment procedure in all buffers (trypsin and PBS) until the cell pellet was placed on ice, since removing rotenone or increasing its content during detachment was found to uncouple mitochondria.

All cultures were routinely checked for mycoplasma contamination and tested negative.

Mitochondria isolation

Mitochondria were isolated from cybrids, MAFs, or mouse heart using a protocol adapted for either cell culture or mouse tissues [28]. Briefly, hearts and liver were cleaned of blood by rinsing in ice-cold phosphate buffered solution (PBS), and the tissue was disrupted with a blade on ice. Disrupted tissue, cybrids, or MAFs were resuspended in a buffer containing 0.32 M sucrose, 10 mM Tris-base and 1 mM EDTA (pH 7.4), placed in a glass Elvehjem potter, and homogenized by up and down strokes using a motor-driven Teflon pestle. Successive homogenization–centrifugation steps yielded the mitochondria-containing fraction, which was quantified with the Bradford protein assay.

Mitochondrial membrane isolation and measurement of complex activities

Mitochondrial membranes from cultured cells or liver were obtained after freeze–thawing isolated mitochondria, and OXPHOS enzyme activity was measured as previously described[29,30], using between 0.5 and 20 µg protein per sample, depending on the activity to be measured. Rotenone-sensitive NADH-ubiquinone decylubiquinone (DQ) oxidoreduction (CI activity) was measured by changes in absorbance at 340 nm. Antimycin A-sensitive succinate-cyt c oxidoreductase activity (CII + CIII activity) was calculated after measuring changes in absorbance at 550 nm. Potassium cyanide (KCN)-sensitive cyt c-oxygen oxidoreductase activity (CIV activity) was calculated after measuring changes in absorbance at 550 nm. Oligomycin-

sensitive ATPase activity (CV activity) was calculated after measuring changes in absorbance at 340 nm driven by the pyruvate kinase reaction coupled to ADP phosphorylation by CV.

Measurement of O_2 consumption and mitochondrial membrane potential

Measurements were made with an O2k Oxygraph instrument (Oroboros Instruments) with the attached fluorescent module. Tetramethylrhodamine methyl ester (TMRM) in quenching mode (2 μM) was used for the detection of mitochondrial membrane potential. Oxygen and TMRM calibration were performed before every experiment. Cells ($2x10^6$) or isolated mitochondria or mitochondrial membranes (50 μg) were loaded in the O2k Oxygraph chambers with Mir05 buffer (Oroboros Instruments) and 20 μg digitonin (only for cells); substrates and inhibitors were added sequentially. Glutamate (10 mM) and malate (0.5 mM) were added to activate CI-dependent respiration and rotenone (0.5 μM) was added to suppress it. Succinate (10 mM) was then added to activate CII-dependent respiration, and subsequently 1 mM ADP was added to activate state 3 respiration; both of which were inhibited by adding 2.5 μM antimycin A. Lastly, 0.5 mM N, N, N′, N′-tetramethyl-p-phenylenediamine (TMPD) and 2 mM ascorbate were added to activate CIV-dependent respiration, which was later suppressed by addition of 100 mM sodium azide. In some experiments, 10 μM cyt c was included in the sequence. In some other experiments, 100 nM nigericin or 100 nM monensin was added after succinate.

Na^+-containing respiration buffer was prepared by replacing potassium phosphate with sodium phosphate in the Mir05 formula (Oroboros instruments). Na^+-free respiration buffer was made with phosphoric acid and buffered to physiological pH with N-methyl D-glucamine (NMDG). Both buffers were compensated in osmolality and ionic strength using NMDG. In addition, in these experiments the acidic forms of substrates, appropriately resuspended in Na^+-free respiration solution and buffered to reach respiration solution pH, were used to avoid the introduction of Na^+ into the Na^+-free respiration buffer or additional Na^+ into the Na^+-containing buffer. Mitochondrial membrane potential was calibrated according to the manufacturer's instructions.

Blue native gel electrophoresis

Complex and supercomplex levels, compositions, and distributions were analyzed in isolated mitochondria by BNGE[31] Mitochondrial proteins were solubilized with 10% digitonin (4 g/g; Sigma-Aldrich D5628) and separated on 3–13%-gradient Blue native gels. Gradient gels (1.5-mm thick) were prepared using a gradient former connected to a peristaltic pump.

SDS gel electrophoresis

Mitochondria were resuspended in RIPA buffer (1% Triton-X-100, 50 mM Tris-HCl pH 7.4, 50 mM sodium chloride, 0.5% sodium deoxycholate, and 5 mM EDTA) supplemented with a protease inhibitors cocktail mix (Sigma P8340). Samples were then incubated at 4ºC on a rotating wheel for 15 minutes and centrifuged for 15 minutes at 13,000 x g at 4ºC. Supernatants were collected and transferred to fresh 1.5 ml Eppendorf tubes. Protein concentration was quantified by the Bradford assay.

The levels and distribution of Opa1 were analyzed by sodium dodecyl sulphate (SDS) gel electrophoresis (SDSGE) on 7.5% gels. Loading buffer (50 mM Tris-HCl pH 6.8, 2% SDS, 10% glycerol, 1% 2-mercaptoethanol, 0.02% bromophenol blue) was added to samples, which were incubated for 5 minutes at 95ºC.

Immunodetection of single proteins, complexes, and supercomplexes

BNGE or SDSGE proteins were electroblotted using a Mini Trans-Blot Cell system (Bio-Rad) onto polyvinylidene difluoride (PVDF) transfer membrane (Immobilon-FL, 0.45 μm; Merck Millipore, IPFL00010) for 1 hour at 100 V in transfer buffer (48 mM Tris, 39 mM glycine, and 20% ethanol). Non-specific binding sites were blocked by incubating membranes with phosphate-buffered saline (PBS) containing 5% bovine serum albumin (BSA) for 1 hour at RT. For protein detection, membranes were incubated in blocking buffer containing primary antibody overnight at 4ºC. After three washes with PBS 0.1 % Tween-20 (PBS-T) for 30 min, membranes were incubated with appropriate secondary antibodies for 1 hour at RT. Membranes were then washed twice with PBS-T and once with PBS. To study complex and supercomplex assembly, the PVDF membrane was sequentially probed with antibodies against CI (anti-NDUFA9, Abcam ab14713), CIII (anti-UQCR2, Proteintech, 14742-1 AP) and CII (anti-Fp70, Invitrogen, 459200). Parallel BNGE western blots were performed to probe CIV (anti-COI, Invitrogen, MTCO1 459600) and CV (anti-ATPβ, Abcam, Ab 14730). To study Opa1 processing, the PVDF membrane was sequentially probed with antibodies against Opa1 (anti-Opa1, Abcam, ab42364) and Fp70 (anti-Fp70, Invitrogen, 459200). Fiji software was used for Opa1 quantification. Antibody binding was detected by fluorescence as previously described[29].

Measurement of mitochondrial ATP synthesis

ATP synthesis was assessed in isolated mitochondria (1.5 to 15 μg mitochondrial protein) using succinate as substrate (plus rotenone) in the presence of ADP in a kinetic luminescence assay based on the luciferin/luciferase reaction[32].

Measurements of mitochondrial matrix Na^+ and H^+

The probe-loading protocol was adapted from[33]. Isolated mitochondria from cells were incubated for 20 min at 37 ºC with 10 μM 2',7'-bis-(2-carboxyethyl)-5-(and-6)-carboxyfluorescein-acetoxymethyl ester (BCECF-AM; for matrix H^+) or with 1,3-benzenedicarboxylic acid, 4,4'-[1,4,10-trioxa-7,13-diazacyclopentadecane-7,13-diylbis(5-methoxy-6,12-benzofurandiyl)]bis-,tetrakis [(acetyloxy)methyl] ester (SBFI-AM; for matrix Na^+). This was followed by two rounds of centrifugation (12000 g, 4ºC, 5 min) and resuspension in sucrose buffer. The last resuspension was in Na^+-free respiration buffer.

Probe-loaded mitochondria were distributed in p96 wells in Na^+-free buffer, unless otherwise indicated. Measurements were made with a Fluoroskan Ascent microplate reader (Thermo Fisher Scientific) at 390/485 nm excitation pair for BCECF-AM and 355/390 nm excitation pair for SBFI-AM. Emission was recorded at 530 nm emission for BCECF-AM and SBFI-AM. Substrates and inhibitors were subsequently added as in the O_2 consumption experiments, without ADP, TMPD, ascorbate, or sodium azide. The H^+ pumping rate was obtained from the slope after adding respiratory substrates; the slope was flat after the addition of the corresponding inhibitors. For the measurement of reverse NHE activity using BCECF-AM, 10 mM NaCl was added after succinate. For measurement of forward NHE activity and Na^+ gradient using SBFI-AM, 10 mM NaCl was added at the beginning of the experiment.

Calibration was performed by adding equal amounts of mitochondria from the same cell type to several wells containing a graded series of pH or Na^+ concentration in the presence of 1 μM nigericin, 1 μM monensin, and 1 μM gramicidin.

Spectrophotometric measurement of NHE activity in isolated mitochondria

The protocol was adapted to the analysis of cell-culture-derived mitochondria from [34]. Briefly, passive mitochondrial swelling was recorded in 50 μg of mitochondria resuspended in 133 mM

sodium acetate, 0.2 mM Tris-EGTA, pH 7.0 at room temperature. Absorbance was recorded at 550 nm in a UV/VISJASCO spectrophotometer (Thermo Fisher Scientific).

In some experiments, sodium acetate was exchanged for sodium chloride as a swelling control. In others, before addition of mitochondria to the sodium acetate buffer, mitochondrial CI was activated by incubating the sample with glutamate/malate in Miro05 buffer for 5 min at 37ºC. Alternatively, mitochondrial CI was deactivated by incubating the mitochondria without substrates in Miro05 buffer for 15 min at 37ºC.

Measurement of Na^+ gradient in whole cells by confocal microscopy

Cytosolic and mitochondrial Na^+ were detected as in[29]. Briefly, cybrids were plated the day before experiments, washed three times with Hank's balanced salt solution with Ca^{2+}/Mg^{2+}/glucose (HBSS + Ca/Mg + glucose), and incubated with 5 µM Asante NaTRIUM Green-2-Acteoxymethyl ester (ANG2-AM) for 30 min at 37 °C in the dark. ANG2-AM was washed out, and new HBSS + Ca/Mg + glucose was added, including 1 µM CoroNa Red. Cells were further incubated for 30 min at 37 °C in the dark. After this, the medium was changed again, cells were washed once with HBSS + Ca/Mg + glucose, and the plate was placed on the automated stage of a Leica SP-5 confocal microscope for live imaging. The planes were focused for image capture, and images were taken with a ×63 objective. Experiments started and ended at 20% O_2 and 5% CO_2. Loaded cells were excited with an argon/krypton laser using the 496-nm line for ANG2-AM and the 514-nm line for CoroNa Red. Fluorescence emission of ANG2-AM was detected in the 515–550-nm range, whereas the emission of CoroNa Red was detected in the 555–575-nm range.

In situ calibration of the same cells was performed after a two-wash step with Na^+-free HBSS + Ca/Mg + glucose. Increasing Na^+ concentrations, starting from 0 mM Na^+, were then applied in the presence of 1 µM nigericin, 1 µM monensin, and 1 µM gramicidin, and images were taken with the excitation/emission wavelengths indicated above. Calibration solutions were equilibrated for at least 5 min.

Measurement of mitochondrial Ca^{2+} in whole cells by confocal microscopy

The protocol followed was exactly as in[29]. Briefly, cells were transiently transfected with Cepia2mt and mitochondrial Ca^{2+} imaged under a Leica SP5 microscope. Mitochondrial Ca^{2+} entry was stimulated by addition of ATP 40 µM and calibrated using ionomycin 1 µM and EDTA 2.5 mM.

Measurement of ΔΨmt in whole cells by confocal microscopy

Cells were seeded the day prior experimentation. Then, cells were incubated with TMRM 50 nM, for non-quenching mode, for 30 min before imaging in a Leica SP5 microscope. Samples were excited with an argon/krypton laser using the 543-nm line and emission was detected in the 555–595-nm range. Calibration was performed following guidelines and indications from PMID: 22495585***.

Measurement of mitochondrial volume

For the determination of mitochondrial volume 50 µg of mitochondria and 1 mL Mir05 respiration buffer were placed in a cuvette, and the absorbance at 550 nm was recorded with a UV/VISJASCO spectrophotometer (Thermo Fisher Scientific). Parallel measurements were taken at steady state and in mitochondria respiring from different substrates for 5 min at 37 ºC. A

valinomycin technical control was included to determine whether this technique was suitable for the measurement of mitochondrial volume changes, with positive results.

Transmission electron microscopy

Cells were analyzed by electron microscopy as previously described[29]. Thin sections including mitochondria were imaged with a JEM1010 electron microscope (Jeol).

Proteomic analysis

Protein extracts of isolated mitochondria from mtDNA^{WT}, ND6^{KO}, ND4^{KO}, NDUFS4^{WT}, and NDUFS4^{KO} samples were obtained by homogenization with ceramic beads (MagNa Lyser Green Beads, Roche, Germany) in CS buffer (Pipes pH6.8, MgCl2, NaCl, EDTA, sucrose, SDS, sodium orthovanadate; Biochain Institute, Inc. #K3013010-5) freshly supplemented with protease and phosphatase inhibitors. Extracted proteins (around 200 µg) from atrial biopsies were subjected to in-filter reduction and alkylation using iodoacetamide followed by trypsin digestion (Nanosep Centrifugal Devices with Omega Membrane-10K, PALL), and the resulting peptides were TMT-labeled according to the manufacturer's instructions. Labeled peptides were subjected to LC-MS analysis using a Proxeon Easy nano-flow HPLC system (Thermo Fisher Scientific, Bremen, Germany) coupled via a nanoelectrospray ion source (Thermo Fisher Scientific) to an Orbitrap Fusion mass spectrometer (Thermo Fisher) using with a 2-cm trap column and a 50-cm analytical column (75 µm I.D, 2 µm particle size, Acclaim PepMap RSLC, 100 C18; Thermo Fisher Scientific) in a continuous acetonitrile gradient consisting of 0-30% A for 60 min, 50-90% B for 3 min (A= 0.1% formic acid; B= 100% acetonitrile, 0.1% formic acid) at a flow rate of 200 nL/min. Mass spectra were acquired in a data-dependent manner, with an automatic switch between MS and MS/MS using a top-speed method and dynamic exclusion. MS spectra were collected in the Orbitrap analyzer using a mass range of 400–1500 m/z at 60,000 resolution. HCD fragmentation was performed at 33 eV of normalized collision energy and MS/MS spectra were analyzed at 30,000 resolution in the Orbitrap.

Proteins were identified with the SEQUEST HT algorithm integrated in Proteome Discoverer 2.5 (Thermo Scientific). MS/MS scans were searched against a pig reference proteome database (human_pig_202105_pro-sw-tr.target-decoy.fasta), (296316 sequences in total). For database searching, parameters were selected as follows: trypsin digestion with 2 maximum missed cleavage sites, precursor mass tolerance of 2 Da, and a fragment mass tolerance of 0.03 Da. Methionine oxidation (+15.994915 Da) and asparagine and glutamine deamidation (+0.984016 Da) were set as variable modifications, whereas cysteine carbamidomethylation (+57.021464 Da) and TMT labeling (+229.162932 Da) at peptide N-terminal ends and Lys residues were considered fixed modifications. False discovery rates (FDR) for peptide identifications were calculated by the refined method[35] with an additional filter for a precursor mass tolerance of 10 ppm[36]. A 1% FDR was used as the criterion used for peptide identification.

Quantitative information from TMT reporter intensities was integrated from the spectrum level to the peptide level and then to the protein level based on the WSPP model[37], using the GIA integration[38].

Statistical analysis

Statistical analyses and graphics were produced with GraphPad Prism 8 software. Datasets were compared by t test, analysis of variance (ANOVA), or nonparametric analysis as appropriate and with P values adjusted for multiple tests. P values from each comparison are shown in every graph. All results are presented as mean ± SD or mean ± SEM.

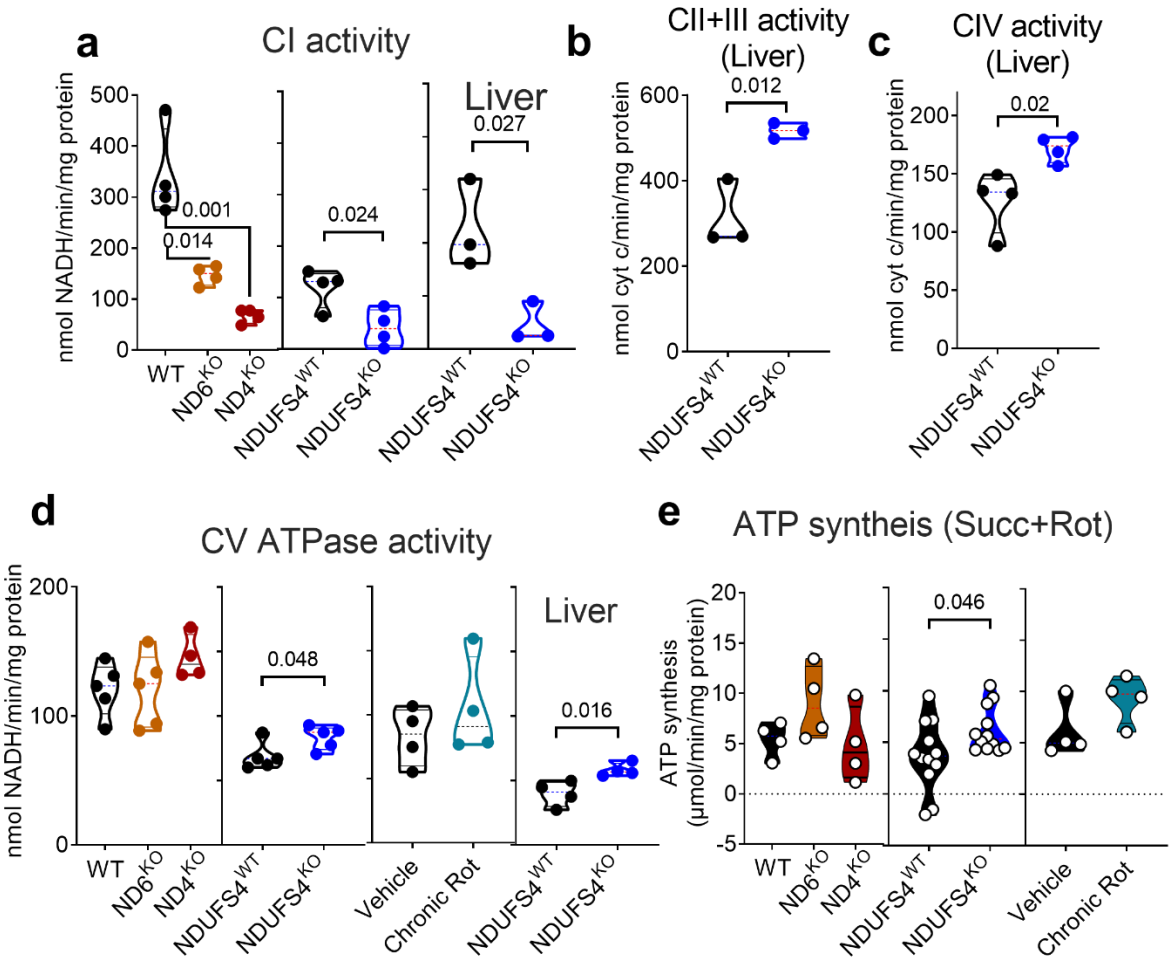

Extended Data Figure 1. Isolated complex activities in CI-deficiency models. (**a**) Rotenone (Rot)-sensitive NADH-CoQ oxidoreductase activity in mtDNA^{WT}, ND6^{KO} and ND4^{KO}, and NDUFS4^{WT} and NDUFS4^{KO} mitochondrial membranes from MAFs and Liver. (**b**) Antimycin A (AA)-sensitive succinate-cyt c oxidoreductase activity in NDUFS4^{WT} and NDUFS4^{KO} mouse liver mitochondrial membranes. (**c**) KCN-sensitive cyt c oxidase activity in NDUFS4^{WT} and NDUFS4^{KO} mouse liver mitochondrial membranes. (**d**) Oligomycin (Olig)-sensitive ATPase activity in mtDNA^{WT}, ND6^{KO}, ND4^{KO}, Vehicle-treated, Chronic rotenone-treated and NDUFS4^{WT} and NDUFS4^{KO} mitochondrial membranes from MAFs and Liver. (**e**) Olig-sensitive ATP synthase activity in mtDNA^{WT}, ND6^{KO}, ND4^{KO}, Vehicle-treated, Chronic rotenone-treated and NDUFS4^{WT} and NDUFS4^{KO} isolated mitochondria in the presence of 1 µM Rot and respiring on succinate.

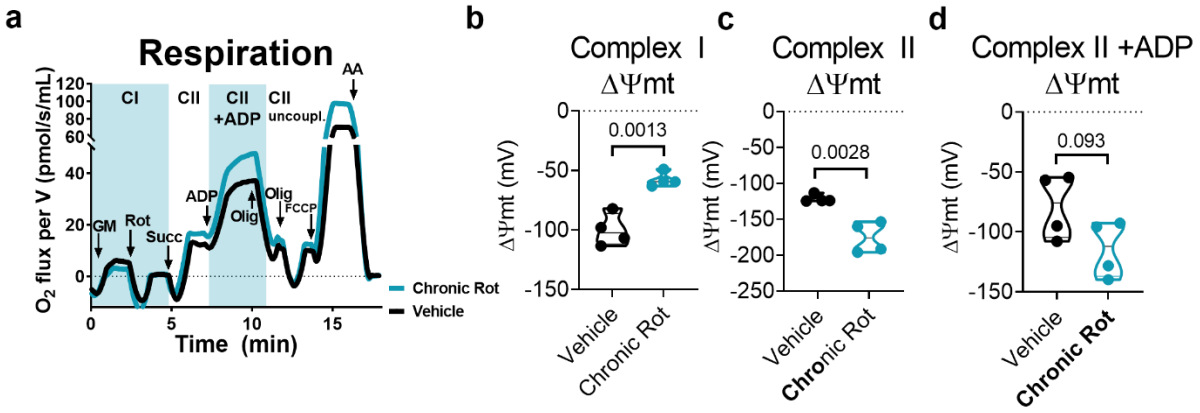

Extended Data Figure 2. Bioenergetics of the Chronic Rot CI-deficiency model. (**a**) Oxygen consumption rates were measured in permeabilized mtDNA^{WT} cells that had been treated with vehicle or Chronic Rot (n=4). Insets and acronyms are the same as those in Fig. 2; FCCP, carbonyl cyanide-p-trifluoromethoxyphenylhydrazone. (**b-d**) Calibrated TMRM signal in permeabilized mtDNA^{WT} cells that had been treated with vehicle or Chronic Rot, respiring on CI substrates (**b**), CII substrates (**C**), or CII substrates +ADP (**d**).

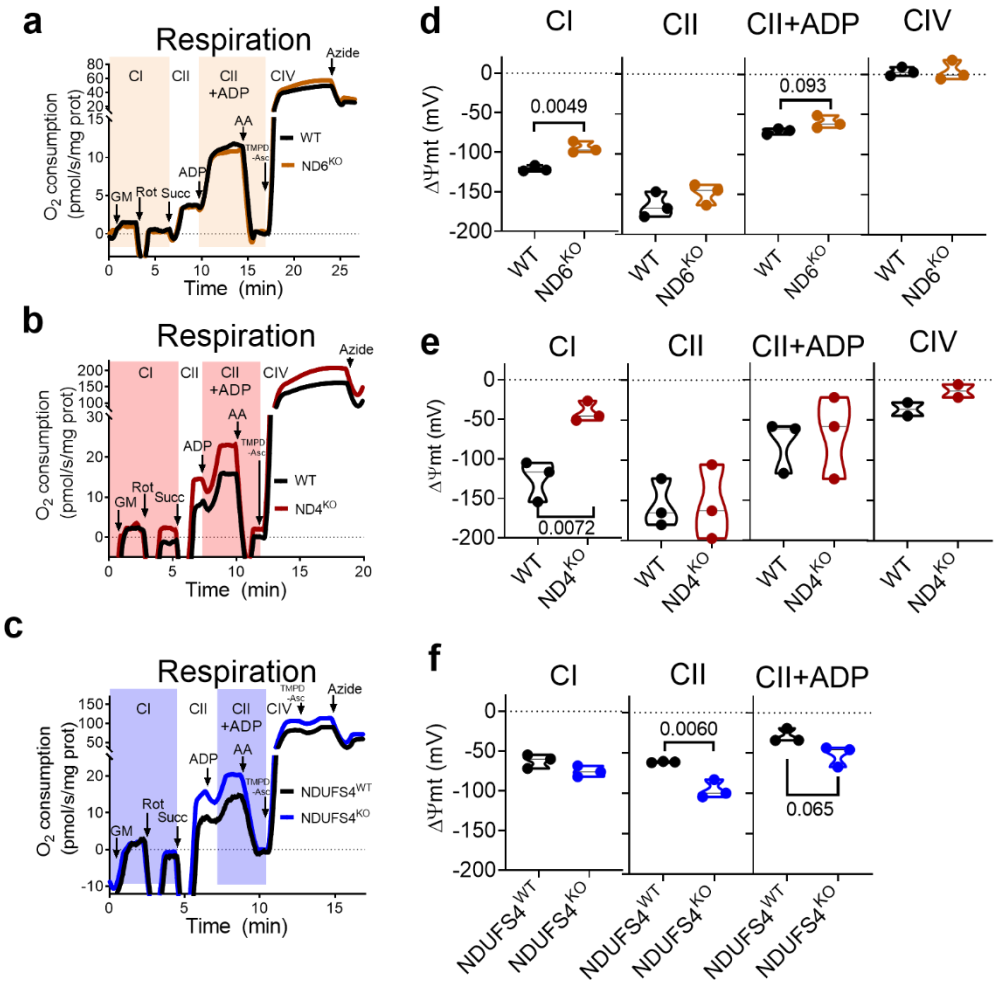

Extended Data Figure 3. Bioenergetics analysis of isolated mitochondria from the CI deficiency models. (**a**) Oxygen consumption rates in isolated mitochondria from mtDNA^{WT} and ND6^{KO} (n=3) cells. (**b**) Oxygen consumption rates in isolated mitochondria from mtDNA^{WT} and ND4^{KO} (n=3) cells. (**c**) Oxygen consumption rates in isolated mitochondria from NDUFS4^{WT} and NDUFS4^{KO} (n=3) cells. Abbreviations are the same as in Fig. 2. (**d**) Calibrated TMRM signal in ND6^{KO}, ND4^{KO} (**e**) and NDUFS4^{KO} (**f**) mitochondira respiring on CI substrates (CI inset), CII substrates (CII inset), CII substrates +ADP (CII+ADP inset), and CIV substrates (CIV inset).

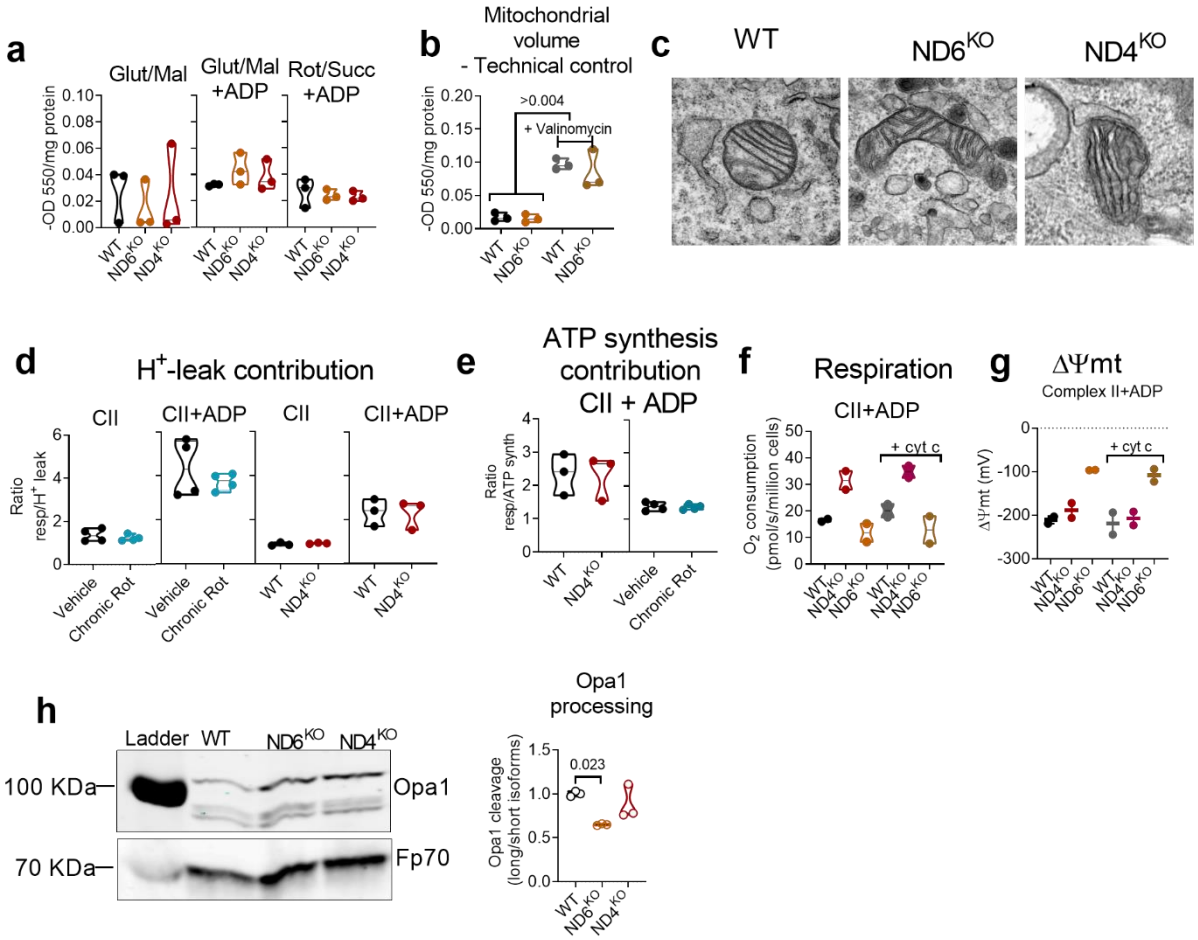

Extended Data Figure 4. ND6^{KO} and ND4^{KO} mitochondria have similar size, H^{+} leak, and MTP permeability to mtDNA^{WT} mitochondria. (**a**) Mitochondrial volume measured by absorbance at 550 nm in the presence of CI substrates (Glut/Mal), CI substrates + ADP (Glut/Mal+ADP), or CII substrates + 1 µM rotenone (Rot/Succ+ADP) in mtDNA^{WT}, ND6^{KO} and ND4^{KO} mitochondria. (**b**) mtDNA^{WT} and ND6^{KO} mitochondrial volume in the absence or presence of valinomycin. (**c**) Transmission electron microscopy (TEM) imaging of mitochondria in mtDNA^{WT}, ND6^{KO}, and ND4^{KO} cells (n=2). (**d**) H^{+} leak contribution to baseline CII respiration +/- ADP in Vehicle and Chronic Rot-treated, as well as in mtDNA^{WT} and ND4^{KO} permeabilized cells, calculated as the ratio of baseline CII respiration (without ADP) to H^{+} leak. (**e**) ATP synthesis contribution to CII respiration in Vehicle and Chronic Rot-treated, as well as in mtDNA^{WT} and ND4^{KO} permeabilized cells, calculated as the ratio of coupled CII respiration (with ADP) to ATP synthesis. (**f**) Oxygen consumption rates in mtDNA^{WT}, ND6^{KO}, and ND4^{KO} permeabilized cells respiring on Succ + Rot + ADP in the absence or presence of cyt c. (**g**) Calibrated TMRM signal in mtDNA^{WT}, ND6^{KO}, and ND4^{KO} permeabilized cells respiring on Succ + Rot + ADP in the absence or presence of cyt c. (**h**) Western blot analysis of OPA1 expression in mtDNA^{WT}, ND6^{KO}, and ND4^{KO} isolated mitochondrial fractions; anti-Fp70 was used as a loading control. Inset: shows quantification of three independent experiments.

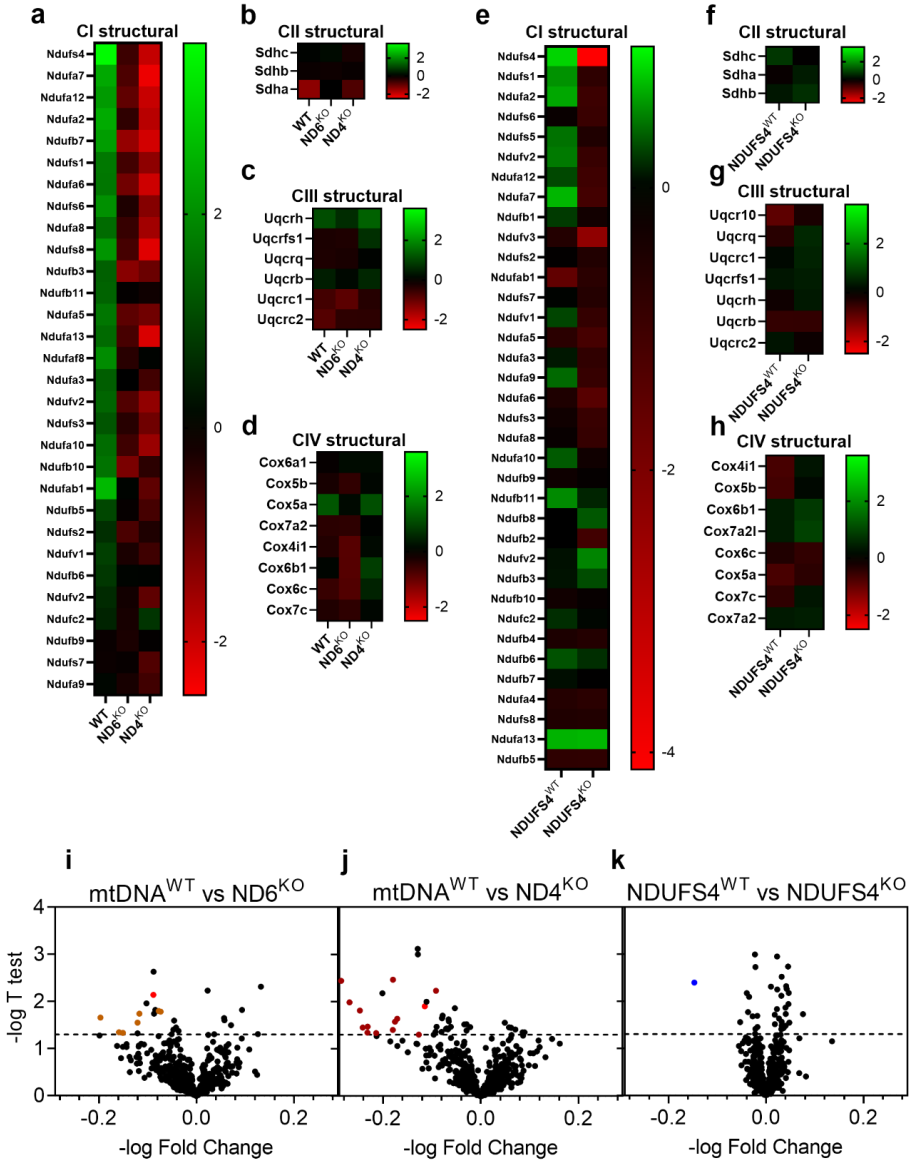

Extended Data Figure 5. Proteomics analysis of mtDNA^{WT}, ND6^{KO}, ND4^{KO}, NDUFS4^{WT}, and NDUFS4^{KO} isolated mitochondria. Relative mean abundances of (**a**) CI subunits in mtDNA^{WT}, ND6^{KO}, and ND4^{KO} mitochondria; (**b**) CII subunits in mtDNA^{WT}, ND6^{KO}, and ND4^{KO} mitochondria; (**c**) CIII subunits in mtDNA^{WT}, ND6^{KO}, and ND4^{KO} mitochondria; (**d**) CIV subunits in mtDNA^{WT}, ND6^{KO}, and ND4^{KO} mitochondria; (**e**) of CI subunits in NDUFS4^{WT} and NDUFS4^{KO} mitochondria; (**f**) of CII subunits in NDUFS4^{WT} and NDUFS4^{KO} mitochondria; (**g**) of CIII subunits in NDUFS4^{WT} and NDUFS4^{KO} mitochondria and (**h**) of CIV subunits in NDUFS4^{WT} and NDUFS4^{KO} mitochondria. (**i-k**) Volcano plot showing relative abundances of all mitochondrial proteins detected in (**i**) mtDNA^{WT} vs ND6^{KO}; (**j**) in mtDNA^{WT} vs ND4^{KO}; (**k**) in NDUFS4^{WT} vs NDUFS4^{KO}. For all experiments, n=3 three independent biological replicates.

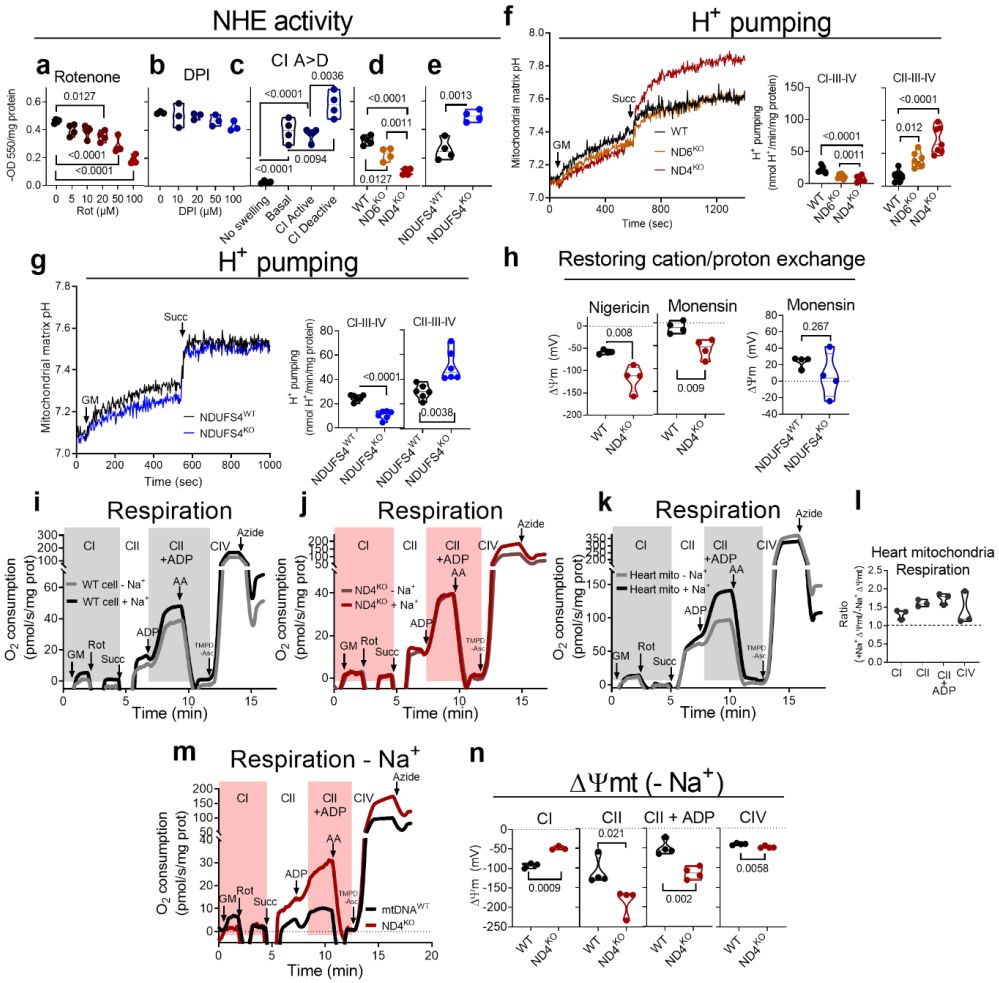

Extended Data Figure 6. CI-NHE activity-dependent Na^+ gradient contributes to total ΔΨmt. (**a**) Dose-response of mouse liver mitochondrial NHE activity to rotenone. (**b**) Dose-response of mouse liver mitochondrial NHE activity to DPI. (**c**) Mouse liver mitochondrial NHE activity in different CI activation states. (**d**) NHE activity in $mtDNA^{WT}$, $ND6^{KO}$ and $ND4^{KO}$ mitochondria. (**e**) NHE activity in $NDUFS4^{WT}$ and $NDUFS4^{KO}$ mitochondria. (**f**) Calibrated BCECF-AM signals of $mtDNA^{WT}$, $ND6^{KO}$ and $ND4^{KO}$ isolated mitochondria under CI (Inset CI-CIII-CIV) and CII substrates (Inset CII-CIII-CIV). (**g**) Calibrated BCECF-AM signals of $NDUFS4^{WT}$ and $NDUFS4^{KO}$ isolated mitochondria under CI (Inset CI-CIII-CIV) and CII substrates (Inset CII-CIII-CIV). (**h**) Calibrated TMRM signal before and after the addition of nigericin (100 nM), monensin (100 nM) in $mtDNA^{WT}$ and $ND4^{KO}$ or monensin (100 nM) in $NDUFS4^{WT}$ and $NDUFS4^{KO}$ isolated mitochondria respiring in Rot/Succ + ADP. (**i-k**) Oxygen consumption rates measured in $mtDNA^{WT}$ (**i**), $ND4^{KO}$ (**j**) and C57BL/6N heart (**k**) mitochondria in Na^+-containing buffer (black or reddish lines) and Na^+-free buffer (gray or brownish lines; n=4). (**l**) Relative contribution of Na^+ to ΔΨmt in C57BL/6N heart mitochondria respiring on CI, CII, CII+ADP, or CIV substrates, calculated as the ratio of the calibrated TMRM signal in Na^+-containing to that in Na^+-free buffer. (**m**) Oxygen consumption rates measured in $mtDNA^{WT}$ and $ND4^{KO}$ mitochondria in Na^+-free buffer (n=4). (**n**) Calibrated TMRM signal in $mtDNA^{WT}$ and $ND4^{KO}$ mitochondria respiring on CI (CI inset), CII (CII inset), CII+ADP (CII+ADP inset), or

CIV (CIV inset) substrates in a Na^+-free buffer. Abbreviations in f, g, i-k and m are the same as those in Fig. 2

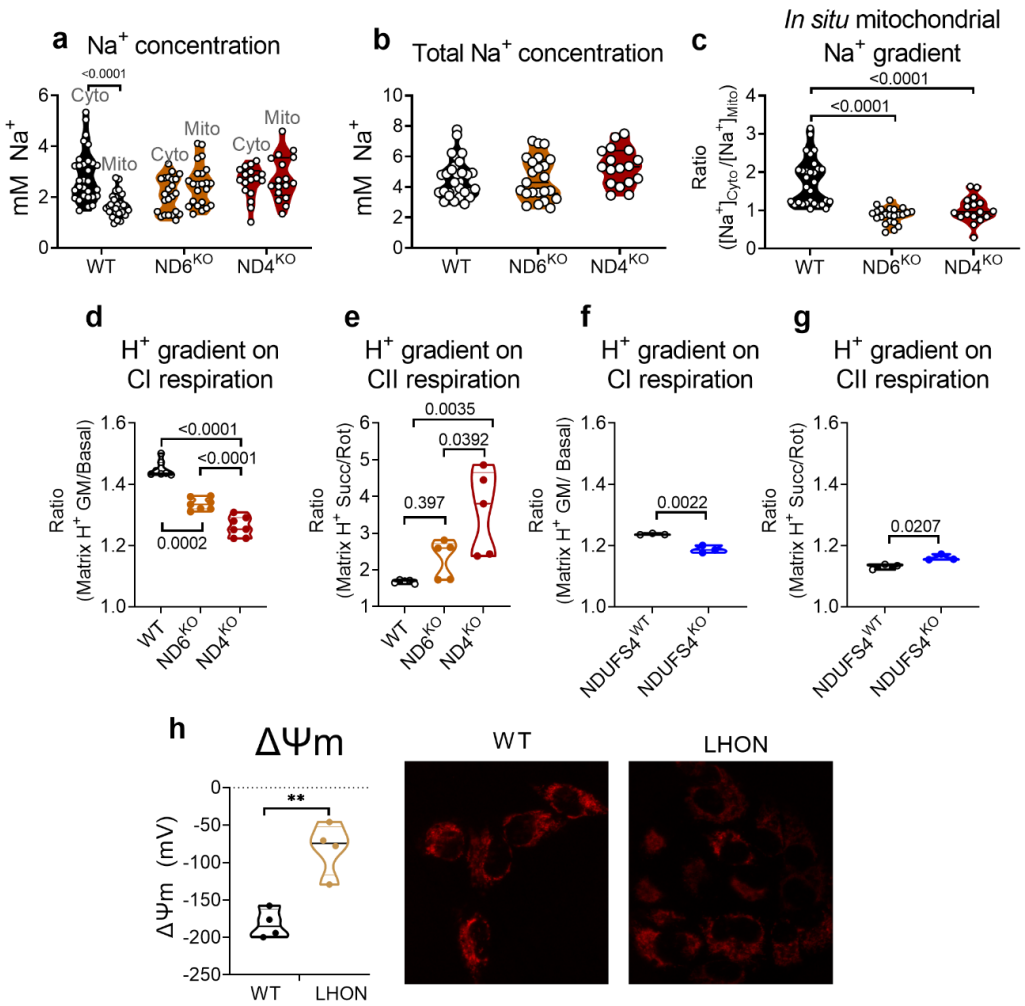

Extended Data Figure 7. The mitochondrial Na^+ gradient parallels the H^+ gradient and contributes to ΔΨmt in intact cells. (**a**) Cytosolic and mitochondrial Na^+ concentrations in $mtDNA^{WT}$, $ND6^{KO}$, and $ND4^{KO}$ intact cells measured by confocal microscopy. (**b**) Total Na^+ concentrations calculated as the sum of cytosolic and mitochondrial Na^+ concentrations, measured by confocal microscopy. (**c**) Mitochondrial Na^+ gradient calculated as the ratio between cytosolic and mitochondrial Na^+ concentrations measured by confocal microscopy. (**d**) H^+ gradient in $mtDNA^{WT}$, $ND6^{KO}$ and $ND4^{KO}$ isolated mitochondria incubated with BCECF-AM and respiring on GM, calculated as the ratio of matrix H^+ concentrations determined after and before addition of rotenone. (**e**) H^+ gradient in $mtDNA^{WT}$, $ND6^{KO}$, and $ND4^{KO}$ isolated mitochondria incubated with BCECF-AM and respiring on succinate + rotenone 1µM, calculated as the ratio of matrix H^+ concentrations determined after and before addition of AA. (**f**) H^+ gradient in $NDUFS4^{WT}$ and $NDUFS4^{KO}$ isolated mitochondria incubated with BCECF-AM and respiring on GM, calculated as the ratio of matrix H^+ concentrations determined after and before addition of rotenone. (**g**) H^+ gradient in $NDUFS4^{WT}$ and $NDUFS4^{KO}$ isolated mitochondria incubated with BCECF-AM and respiring on succinate + rotenone 1µM, calculated as the ratio of matrix H^+ concentrations determined after and before addition of AA. (**h**) Calibrated TMRM signal measured by confocal microscopy in intact control vs LHON cybrids.

Comparisons vs Control	CII+III activity	CIV activity	CV activity	Respiration	ΔΨmt
ND6^{KO}	Higher (Fig. 2c)	Equal (Fig. 2g)	Equal (ED Fig. 1d-e)	Equal (Fig. 3a and ED Fig. 3a)	Equal (Fig. 3d and ED Fig. 3d)
ND4^{KO}	Higher (Fig. 2d)	Higher (Fig. 2h)	Equal (ED Fig. 1d-e)	Higher (Fig. 3b and ED Fig. 3b)	Equal (Fig. 3e and ED Fig. 3e)
NDUFS4^{KO}	Higher (Fig. 2e)	Higher (Fig. 2i)	Higher (ED Fig. 1d-e)	Higher (Fig. 3c and ED Fig. 3c)	Hyperpolarized (Fig. 3f and ED Fig. 3f)
Chronic Rot	Higher (Fig. 2f)	Equal (Fig. 2j)	Equal (ED Fig. 1d-e)	Higher (ED Fig. 2a)	Hyperpolarized (ED Fig. 2c and d)

Extended Data Table 1. Summary of bioenergetics characterization of CI-deficiency models.

	Estimation approach	Na^+-dependent ΔΨmt (mV)	Contribution to ΔΨmt (%)
CI respiration (isolated mitochondria)	ΔΨmt measurement in $mtDNA^{WT}$± Na^+	-92.78 ± 27.31	34.72 ± 6.35
CII respiration (isolated mitochondria)	ΔΨmt measurement in $mtDNA^{WT}$± Na^+	-157.46 ± 37.89	34.49 ± 5.74
CII+ ADP respiration (isolated mitochondria)	TMRM fluorescence ± monensin	-86.14 ± 16.97	53.11 ± 5.79
	ΔΨmt measurement in $mtDNA^{WT}$± Na^+	-111.06 ± 16.93	

Extended Data Table 2. Summary of total and relative contributions of the Na^+ gradient to ΔΨmt in the presence of different respiratory substrates and oxidizing conditions.